Article

Ceria-Spiderweb Nanosheets Unlock the Energy-Storage Properties in the "Sleeping" Triplite (Mn$_2$(PO$_4$)F)

Nkosikhona Nzimande, Aderemi Haruna, Patrick Mwonga, Bertold Rasche, Franscious Cummings, and Kenneth I. Ozoemena*

Read Online

ACCESS | Metrics & More | Article Recommendations | Supporting Information

ABSTRACT: Rechargeable aqueous mobile-ion batteries (RAMIBs) are attractive next-generation battery technologies. Manganese fluorophosphate (triplite), Mn$_2$(PO$_4$)F (MFP), and its ceria- and carbon-coated composites (i.e., MFP-CeO$_2$ and MFP-C-CeO$_2$), have been synthesized using a microwave-assisted hydrothermal process. The materials are thoroughly characterized using powder X-ray diffraction, Raman spectroscopy, X-ray photoelectron spectroscopy, high-resolution transmission electron microscopy, high-resolution scanning electron microscopy (field-emission scanning electron microscopy), and energy-dispersive X-ray spectroscopy elemental mapping to prove the successful synthesis of the materials and confirm their morphologies and elemental compositions. These materials have been used to introduce environmentally friendly and low-cost ceria-enabled rechargeable aqueous sodium-ion batteries (CERASIBs) using zinc foil as the anode and sodium perchlorate as the "water-in-salt" electrolyte. The batteries offer a high voltage window (1.6−2.2 V), with MFP-C-CeO$_2$ giving a higher specific capacity of ∼195 mAh g^{-1} than MFP-CeO$_2$ (∼100 mAh g^{-1}). However, MFP-CeO$_2$ showed excellent cycling stability (ca. 99% capacity retention) compared to MFP-C-CeO$_2$ (ca. 78% capacity retention) after 300 cycles due to the impressive structural stability of the MFP material, aided by the ceria coating. The difference in the electrochemical properties of the two materials is related to their different morphologies: the MPF-CeO$_2$ material comprises micron-sized particles that consist of aggregated nanoparticles, while the MPF-C-CeO$_2$ material exhibits mostly a nanoporous structure. The remarkable properties of the CERASIB promise to open doors of opportunities for the design and manufacturing of various lanthanoid- or rare-earth metal compound-enabled triplite-based cathode materials for the large-scale development of affordable RAMIBs involving various mobile ions (such as Na, Li, K, Zn, Mg, and Al) and accompanying zinc anode materials.

KEYWORDS: triplite, manganese fluorophosphate (Mn$_2$(PO$_4$)F), ceria (CeO$_2$) coating, microwave-assisted synthesis, water-in-salt electrolyte, aqueous sodium-ion batteries, energy storage
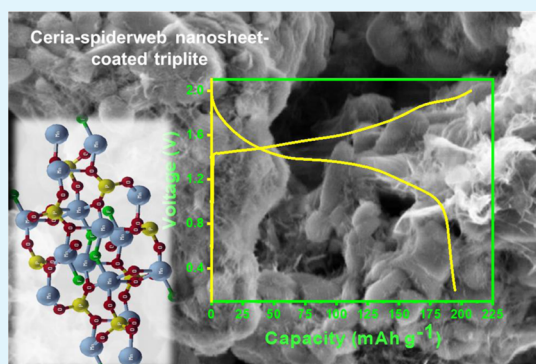
1. INTRODUCTION

Rechargeable batteries are crucial for the development of next-generation consumer electronics, electric vehicles, and stationary/home-electricity storage application and storage of renewable energy sources (especially solar and wind). Lithium-ion batteries (LIBs) dominate the market for energy storage due to their advantage of high energy density.[1−3] However, the general concern for LIBs (such as safety issues due to high flammability/fire hazards, limited availability, and nonuniform distribution of lithium) calls for the need for alternative battery technologies.

Rechargeable aqueous metal-ion batteries (RAMIBs) have continued to receive huge global attention as potential alternatives to state-of-the-art commercial batteries (e.g., lead-acid, Ni−MH, and Ni−Cd).[4] RAMIBs are safe, environmentally friendly, high ionic conducting, and cheap. Some of the most promising RAMIBs are the sodium-ion batteries (SIBs),[4−7] zinc−air batteries,[8] zinc-ion batteries (ZIBs),[4,9] and

sodium−zinc (Na−Zn) hybrid battery systems.[4,10] Sodium (Na) is outstanding as it is hugely abundant (i.e., the fourth most abundant element in the earth's crust) and, unlike lithium, is uniformly distributed around the world. SIB represents the most attractive alternative to lithium-ion batteries (LIBs), especially for stationary or home-electricity storage applications. In addition, zinc metal represents an ideal anode material for aqueous batteries[11,12] due to its many inherent advantages; for example, it exhibits high theoretical specific capacity (820 mAh g^{-1}), low potential (−0.762 V vs standard hydrogen electrode (SHE)), and relatively high

overpotential (−1.06 V vs SHE) for a hydrogen evolution reaction (HER) to take place, which means that it is more difficult for an aqueous electrolyte to decompose via water splitting when a Zn anode is employed, thus conferring to zinc-based aqueous batteries more durable cycling performance. Besides being highly abundant (i.e., 24th most abundant element in the earth's crust), low toxic, intrinsically safe, it is highly sustainable as it is durable and recyclable, thus justifying its use in this work as the anode. Most RAMIBs based on Na-ion technology operate at a low voltage (i.e., low energy density) of about 1.2 V[4], in contrast to the slightly higher voltage ($\approx$1.5 V) observed in this work.

In this work, we report a new, safe, environmentally friendly, low-cost, and ceria-enabled sodium-ion battery (CERASIB) using manganese fluorophosphate, $Mn_2(PO_4)F$ (abbreviated herein as MFP) as the cathode material. $Mn_2(PO_4)F$ is a member of the triplite family, which is a rare phosphate mineral with chemical formula $(Mn,Fe)_2(PO_4)(F,OH)$. Although MFP was first reported in 1972 by Rea and Kostiner,[13] this is the first time it has been found to be an efficient material for the development of RAMIBs. MFP is synthesized, for the first time, using a simple, low-cost microwave-assisted process. We show that MFP exhibits unique properties compared to other RAMIBs reported to date. First, the MFP coated with ceria nanosheets (cathode), combined with zinc foil as the anode, with a sodium-based aqueous electrolyte can provide an average voltage of 1.6 V as a RAMIB, with a high specific capacity of ~195 mAh g^{-1}. Second, Mn-based materials are well known as important supercapacitor[14−16] and battery cathode materials[17−19] and are hugely naturally abundant (especially in South Africa, which controls 80% of the global manganese reserves[20]). The combined advantages of Mn, Na, and Zn (especially low cost, safe to use, and environmentally benign) promise to make the MFP-based RAMIB one of the next-generation energy-storage technologies.

The choice of ceria as a coating agent in this work is based on its interesting advantages in energy-storage electrode materials: improved structural stability (leading to cycling stability, capacity retention) and enhanced rate capability. For example, it has been reported that a moderate amount of ceria coating (usually 2 wt %) provided the optimum performance for LiFePO$_4$/C[21] and Li[Ni$_{0.5}$Co$_{0.2}$Mn$_{0.3}$]O$_2$[22] cathode materials for lithium-ion batteries and Na$_{0.67}$Co$_{0.25}$Mn$_{0.75}$O$_2$ cathode material[23] for sodium-ion batteries. These advantageous properties of CeO$_2$ may be related to its inherent physicochemical properties of high hardness,[24] good protection against corrosion, and good thermal stability, good ionic conduction, reversible oxygen storage, and catalytic activity.[25] Unlike in this work, however, there is no literature precedent on the use of ceria or rare-earth metal compounds activating an electrode material to achieve energy-storage properties. Also, hitherto, there is no literature report that the triplite material (Mn$_2$(PO$_4$)F) exhibits electrochemical energy-storage properties.

2. EXPERIMENTAL SECTION

2.1. Chemicals and Materials. Sodium fluoride (NaF), ammonium dihydrogen phosphate (NH$_4$H$_2$PO$_4$), manganese nitrate tetrahydrate (Mn(NO$_3$)$_2$·4H$_2$O), cerium nitrate hexahydrate (Ce-(NO$_3$)$_3$·6H$_2$O), potassium hydroxide, carbon black (CB), poly-(vinylidene fluoride), sodium perchlorate, and N-methyl-2-pyrroli-

done were purchased from Sigma-Aldrich and were used without any purification.

2.2. Synthesis of Pristine Triplite Mn$_2$PO$_4$F (MPF). The synthesis process for MPF is summarized in the Supporting Information (Figure S1). About 125.96 mg of NaF (3 mmol) and 230.06 mg of NH$_4$H$_2$PO$_4$ (2 mmol) were dissolved in 10 mL (separate beakers) of deionized water and left to stir for ~20 min to be fully dissolved. The NH$_4$H$_2$PO$_4$ solution was then poured into the beaker that contained NaF, forming a clear solution (solution A). For the preparation of solution B, 502.01 mg of Mn(NO$_3$)$_2$·4H$_2$O (2 mmol) was dissolved in 20 mL of deionized water and left to stir for ~10 min to be fully dissolved. Solution A was gradually added to solution B and properly mixed, forming a gel-like whitish solution that was left to stir for ~12 h at 1000 rpm and room temperature. The solution was subjected to microwave-assisted hydrothermal synthesis at 600 W, 180 °C, and 50 bar under constant stirring, first ramped up for 10 min and then ran for 45 min. The resulting product was tortilla brown in color, which was then centrifuged five times with water and then three times with ethanol, left to dry at 60 °C for 12 h, preheated at 350 °C for 4 h in a tube furnace, and then annealed at 800 °C for 8 h under Ar at a flow rate of 0.072 L min^{-1}. The final MPF product was a tortilla to peanut brown in color.

2.3. Synthesis of MPF-CeO$_2$. The synthesis process for MPF-CeO$_2$ is summarized in the Supporting Information (Figure S1). About 500 mg of pristine MPF was added to a solution containing 25.23 mg of Ce(NO$_3$)$_3$·6H$_2$O in 50 mL of deionized water, and a coffee brown solution was formed. The mixture was kept under stirring for 30 min and then sonicated for 30 min at 25 °C. The solution was adjusted to pH 12 with 2 M KOH and vigorously stirred for 2 h, forming a mocha brown solution. The product was centrifuged with deionized water until neutral pH, then dried at 60 °C for 12 h, and subsequently heated under an air tube furnace at 250 °C for 2 h, obtaining a wood to carob brown product. The product was annealed at 800 °C for 8 h under Ar at a flow rate of 0.072 L min^{-1}.

2.4. Synthesis of MPF-C-CeO$_2$. About 503.86 mg of NaF (3 mmol), 920.24 mg of NH$_4$H$_2$PO$_4$ (2 mmol), and 882.58 mg of citric acid were separately dissolved in 10 mL of deionized water and left to stir for ~20 min to be fully dissolved. Then, a solution containing NH$_4$H$_2$PO$_4$ was poured into the beaker containing NaF to make solution A, forming a clear solution. For preparation of solution B, 2.0 g of Mn(NO$_3$)$_2$·4H$_2$O (2 mmol) was dissolved in 20 mL of deionized water and left to stir for ~10 min to be fully dissolved. Solution A was gradually added to solution B, which upon mixing gave a gel-like whitish solution. This was stirred for 6 h and the solution containing citric acid was subsequently added to make up solution C, with no color change being observed. Solution C was stirred for another 6 h at 1000 rpm at room temperature. Microwave-assisted hydrothermal synthesis was carried out as described before for MPF. Then, 524.90 mg of the as-prepared MPF-C was added to a solution containing 26.49 mg of Ce(NO$_3$)$_3$·6H$_2$O in 50 mL of deionized water, forming a carob brown solution. The mixture was stirred for 30 min and then sonicated for 30 min at 25 °C. The solution was adjusted to pH 12 with 2 M KOH and vigorously stirred for 2 h, forming a pure brown solution. The product was centrifuged with water until neutral pH, then dried at 60 °C for 12 h, and subsequently heated in air with a tube furnace at 250 °C for 2 h,[8] obtaining a brown product that was then annealed at 800 °C for 8 h under an Ar atmosphere at a flow rate of 0.072 L min^{-1}.

2.5. Physical Characterizations. Powder X-ray diffraction (PXRD) patterns were collected using a Bruker D8-advance with a Cu Kα_1 = 0.154060 nm radiation source; the range was 15° ≤ 2θ ≤ 110° in a 0.015° measurement step. The refinement data was analyzed using TOPAS software. Raman data was collected using a 514.5 nm (green) line from our Lexel model 95 SHG argon-ion laser. Fourier transform infrared (FTIR) was carried out using a Bruker Vector 22 FTIR spectrometer collected within the range of 500−4000 cm^{-1}. Nitrogen adsorption and desorption (Brunauer−Emmett−Teller (BET)) isotherms were collected using N$_2$ gas by desorption and adsorption using a Micromeritics Tristar 3000 instrument at 77 K; the
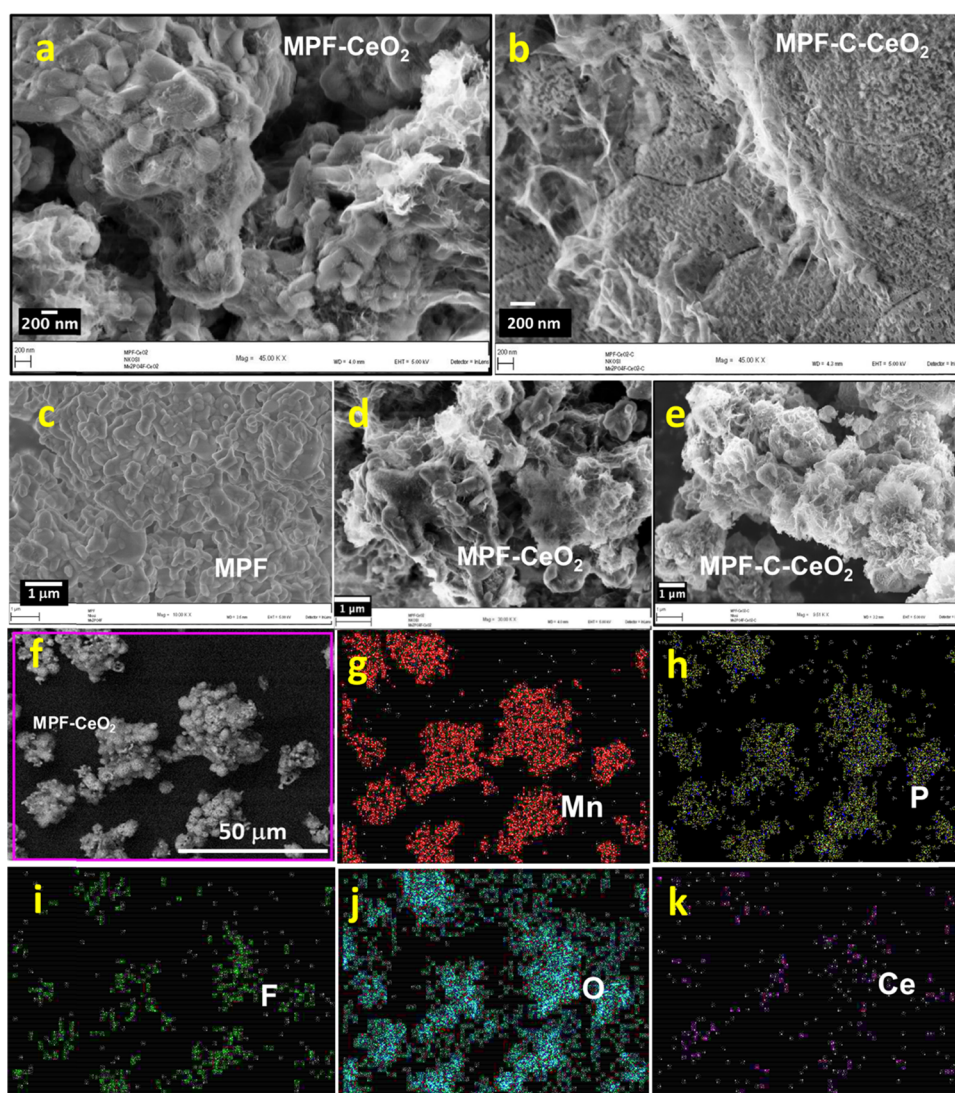
Figure 1. High-magnification (200 nm) SEM images of (a) MPF-CeO$_2$ and (b) MPF-C-CeO$_2$; low-magnification (1 μm) SEM images of (c) MPF, (d) MPF-CeO$_2$, and (e) MPF-C-CeO$_2$; and EDX elemental color mapping results of (f) MPF-CeO$_2$ showing uniform distribution of (g) Mn, (h) P, (i) F, (j) O, and (k) Ce.

samples were degassed before analysis using N$_2$ at 423−473 K. Scanning electron microscopy (SEM) images were collected with an FEI Nova 600 instrument at 30 kV using gold and carbon for plating. Bright-field transmission electron microscopy (TEM) images were collected with a Tecnai Spirit T12 at 120 keV. A Tecnai G^{2}20 field-emission microscope, operated at 200 keV, was employed for high-resolution analysis. In both instances, 2 mg of sample was dispersed in 5 mL of ethanol by ultrasonication for about 15 min. Two drops of the solution were drop-cast on a lacey carbon-coated copper grid, followed by drying at ambient temperature before commencing the analysis. X-ray photoelectron spectroscopy (XPS) measurements were recorded at NMISA using a Thermo ESCAlab 250Xi monochromatic Al Kα (1486.7 eV), 300 W (X-ray power), 900 μm (X-ray spot size), 100 eV (pass energy survey), and 20 eV (pass energy Hi-res) at <10−8 mbar.

2.6. Device Fabrication and Electrochemical Measurements. The cathode was prepared by mixing the active material (i.e., MFP, MFP-CeO$_2$, or MFP-C-CeO$_2$), carbon black (CB) (TIMCAL SUPER C45 Carbon Black) as a conducting agent, and poly(vinylidene fluoride) (PVDF, Sigma-Aldrich) as the binding agent, with a weight ratio of 80:15:5 to form a homogeneous slurry. A few milliliters of N-methyl-2-pyrrolidone (Sigma-Aldrich) was added to the mixture and magnetically stirred for 24 h. The slurry was uniformly spread onto carbon paper (AvCarb P50, Fuel Cell Stores)

and dried under vacuum for 12 h. Full cell configurations were studied using a Swagelok T-type electrochemical cell, with the MFP-based materials as the cathode, zinc foil as the anode, glass microfibre filters (Whatman GF/F) as the separator, and 4 M aqueous NaClO$_4$ as the electrolyte. The capacity was measured with respect to the mass of the active electrode materials (∼3 mg cm^{-2}). All electrochemical measurements were performed with a Bio-Logic SP300 potentiostat and BCS-800 battery cycler series driven by EC-Lab 11.3 BT-lab 11.2 software at room temperature and included cyclic voltammetry (CV), constant current charge−discharge (CD), and electrochemical impedance spectroscopy (EIS). EIS measurements were carried out with a potential amplitude of 5 mV at frequencies from 100 kHz down to 10 mHz at open-circuit voltage perturbation. Each cell was scanned multiple times to ensure that a stable voltammogram was obtained before actual measurements were recorded.

3. RESULTS AND DISCUSSION

3.1. Synthesis and Physical Characterization. The triplite, manganese fluorophosphate, Mn$_2$(PO$_4$)F (herein abbreviated as MPF) is a rare phosphate mineral, first reported about 50 years ago (1972) by Rea and Kostiner,[13] researchers at the Cornell University, USA. These researchers adopted a
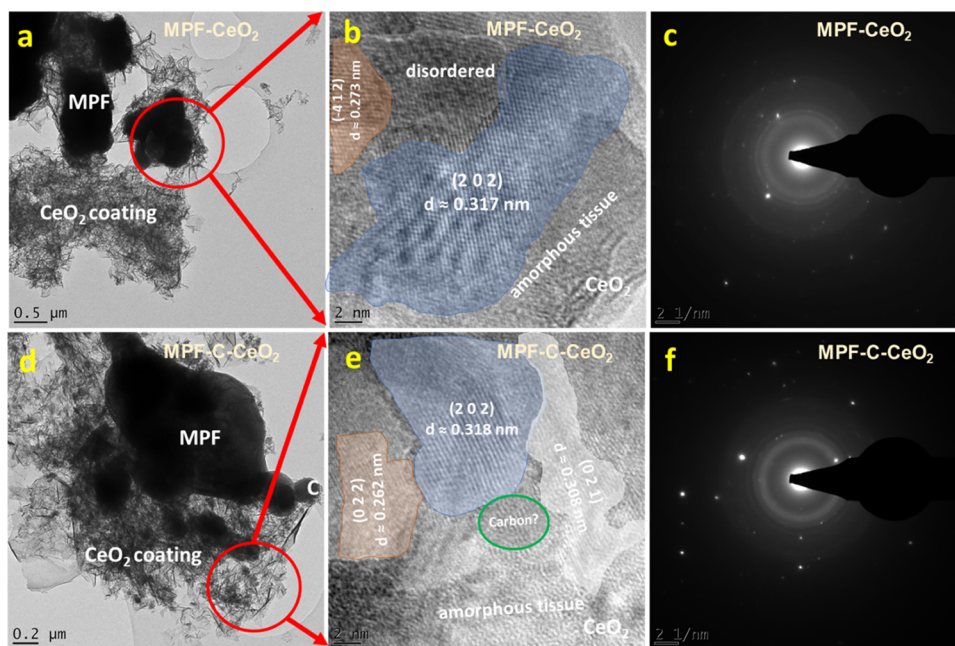
Figure 2. (a) Bright-field TEM image, (b) HRTEM, and (c) selected area electron diffraction (SAED) pattern of MPF-CeO$_2$ and (d) bright-field TEM image, (e) HRTEM, and (f) SAED pattern of MPF-C-CeO$_2$.

somewhat complicated (energy-intense and costly) synthesis method to obtain single crystals of MPF, involving the heating of the precursors, excess amount of MnF$_2$ as a flux, and Mn$_3$(PO4)$_2$ in a platinum crucible at a high temperature of 1150 °C under a nitrogen environment. Until now, there is no knowledge of electrochemistry nor the energy-storage capability of the MPF. In this work, microwave-assisted synthesis has been adopted to synthesize MPF using easily available precursors (hydrated manganese nitrate, ammonium phosphate, and sodium fluoride) and a little amount of ceria (∼2 wt %) as a coating agent (Figure S1).

Figure 1 presents the typical high-resolution SEM images of (a) MPF-CeO$_2$ and (b) MPF-C-CeO$_2$, with the latter showing a more porous morphology than the former. Unlike the pristine MPF (Figure S2), the MPF-CeO$_2$ samples are completely covered with spiderweb-like nanosheets formed by coating them with about 2% ceria (refer to the Experimental Section for detail). The MPF-CeO$_2$ material (Figure 1a) is made up of micron-sized particles that consist of aggregated nanoparticles (80−300 nm), while the MPF-C-CeO$_2$ material (Figure 1b) exhibits mostly nanoporous structure covered with ceria spiderweb nanosheets. The morphologies of the materials are further clarified at low magnifications (Figure 1c−e) and in the Supporting Information (Figure S2). The energy-dispersive X-ray (EDX) elemental color mapping for MPF-CeO$_2$ (Figure 1f−k) shows uniform distribution of Mn, P, F, O, and Ce within the entire porous structure. Similarly, both MPF and MPF-C-CeO$_2$ show uniform distribution of elements (Figures S3 and S4).

Figure 2 compares the high-resolution TEM (HRTEM) images of MPF-CeO$_2$ and MPF-C-CeO$_2$. It was difficult to capture clearly defined HRTEM images (and hence lattice fringes) of the pristine MPF due to its large thickness (Figure S5); however, it was possible to obtain a lattice fringe with a d-spacing of roughly 0.525 nm, which is close to the calculated 0.533 nm for (011) (refer to crystallographic data of triplite,

Mn$_2$PO$_4$F, reference code 01-072-1403) in accordance with the structure of MPF by Waldrop.[26]

Figure 2a shows the bright-field TEM micrograph of MPF-CeO$_2$, while Figure 2b shows the corresponding high-resolution image of the area circled in (a). The calculated d-spacings of 0.273 and 0.317 nm are indexed to the (202) and ($\bar{4}$11) facets, respectively. As expected from the low temperature (250 °C) used in the ceria coating, the ceria nanosheets appear mostly as amorphous tissues. The well-defined rings of the SAED patterns (Figure 2c) come from crystalline regions of the MPF-CeO$_2$, while the diffuse discs in the diffraction patterns emerged from amorphous regions. The bright spots come from the isolated crystalline regions in the MPF; however, these are almost impossible to index as they are randomly scattered.

The thickness of the CeO$_2$ coating, from both SEM and HRTEM measurements, ranges 291 nm and 3.56 μm. Figure 2d−f shows the bright-field TEM micrograph, high-resolution TEM micrograph, and SAED pattern of the MPF-C-CeO$_2$, respectively. The HRTEM images of MPF-C-CeO$_2$ follow similar patterns to those for MPF-CeO$_2$ (Figure 2a−c) except that more amorphous tissues are seen with MPF-C-CeO$_2$ attributed to the presence of carbon. In addition, the calculated d-spacings of 0.318, 0.308, and 0.262 nm are easily indexed to the (202), (021), and (022), respectively. Quite a few regions look like carbon quantum dots (indicated by the green circle, Figure 2e) of about 2 nm in diameter, which also contribute to the diffuse rings observed in the SAED pattern of Figure 2f.

From the PXRD comparison of the three samples (Figure 3), MPF (Figure 3b), MPF-CeO$_2$ (Figure 3c), and MPF-C-CeO$_2$ (Figure 3d) exhibit the same peak positions as the mineral triplite (Figure 3a) and even sharper peaks at 24.30° ($\bar{3}$11), 31.33° (220), and 55.47° (431) than the mineral triplite. In addition, Rietveld fits of the PXRD patterns (Figure 3e−g) confirm that phase-pure Mn$_2$PO$_4$F was successfully synthesized as all of the Bragg peaks could be fully indexed to the crystal structure of the monoclinic symmetry correspond-
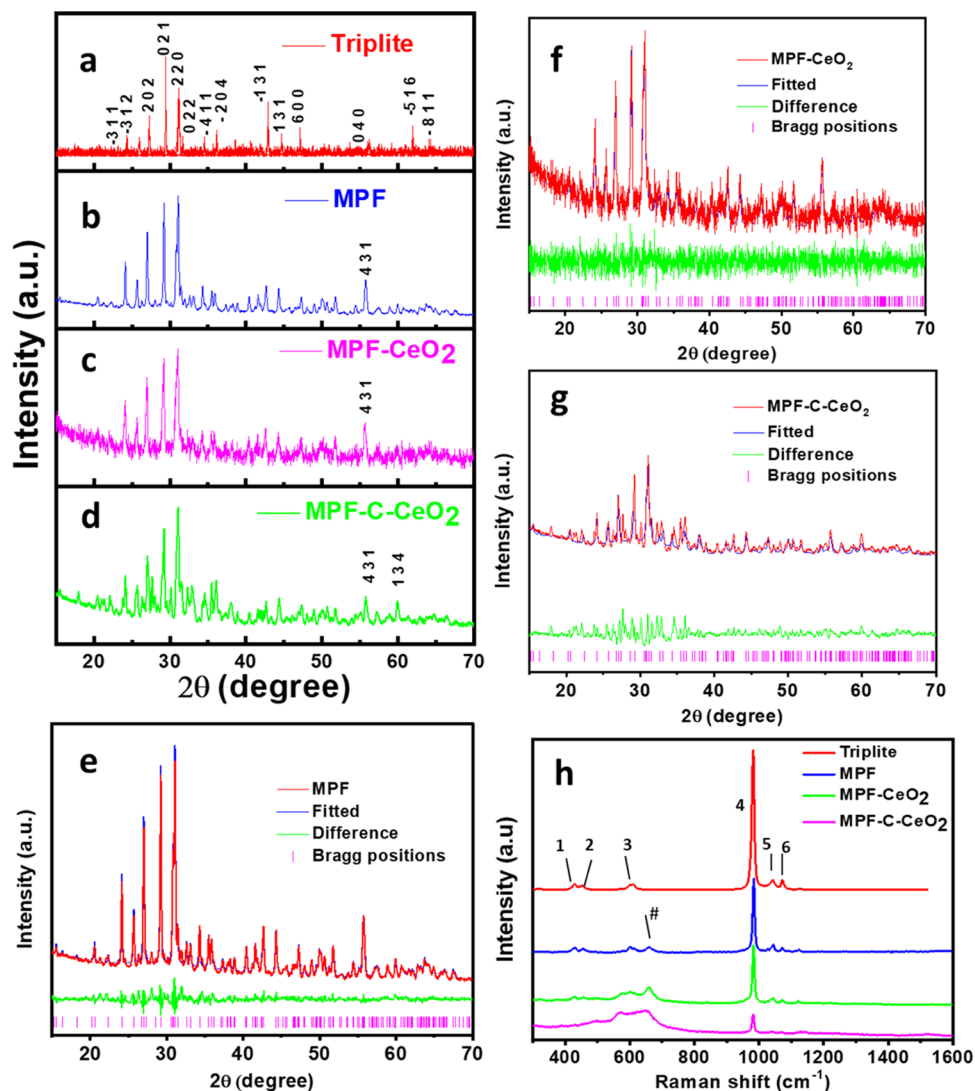
Figure 3. Comparison of the PXRD patterns of (a) mineral triplite, (b) MPF, (c) MPF-CeO$_2$, and (d) MPF-C-CeO$_2$; Rietveld fits of the PXRD patterns of (e) MPF, (f) MPF-CeO$_2$, and (g) MPF-C-CeO$_2$; and comparison of the (h) Raman spectra of mineral triplite, MPF, MPF-CeO$_2$, and MPF-C-CeO$_2$.

ing to the space group $C2/c$ (15), corroborating the crystallographic data of triplite Mn$_2$PO$_4$F that was first structurally elucidated in 1972 by Rea and Kostiner.[13]

In addition, it can be deduced that coating with CeO$_2$ does not cause any significant changes in the phase or peak positioning of the original MPF. From the Rietveld refined peaks, the lattice parameters (Table S1) are essentially the same as previously reported.[13] These results reveal that upon incorporation of ~2% CeO$_2$ coating the lattice parameters changed by 0.1%, meaning that the coating does not significantly affect the lattice positions of the atom but maintains the integrity of the material.

The Raman spectra for the MPF, MPF-CeO$_2$, and MPF-C-CeO$_2$ (Figure 3h) obtained using 514.5 nm (green line) gave the expected Raman bands (summarized in Table S2). All of the samples are dominated by the phosphate group with a very sharp and strong Raman band centered at 980.5 cm^{-1} (i.e., ν1 vibration symmetric stretching of the phosphate unit). The medium band for triplite at around 1036 cm^{-1} (i.e., ν2 asymmetric vibration stretching of the phosphate unit) is observed in the samples in the 1043–1044 cm^{-1} region. The

weak band occurring at 1072 cm^{-1} for triplite (i.e., ν3 asymmetric stretching of the phosphate unit) is also found in the samples in the 1071–1076 cm^{-1} region.

The bands within the range 429 and 458 cm^{-1} correspond to ν2 phosphate deformation, while those in the 600–610 cm^{-1} region correspond to ν4 phosphate deformation. In summary, the Raman spectrum data corroborate the PXRD data that the synthesized materials are triplite MPF materials. The FTIR data (Figure S6) are characterized by absorption bands located in the 400–650 cm^{-1} region, corresponding to the phosphate bond vibration as well as lattice vibrations and stretching vibrational modes of the phosphate tetrahedra in the 1200–900 cm^{-1} region, which agrees with the literature for triplite.[27]

The nitrogen adsorption−desorption isotherm plots (Figure S7 and Table S3) reveal a type IVa classification, characteristic of mesoporous materials. At pressures 0.8−1.0, a small type H1 hysteresis loop was observed, which is associated with capillary condensation in the mesopores. This hysteresis is characteristic of materials with pore sizes wider than ~4 nm, which, incidentally, all of the three materials exceed: MPF-C-CeO$_2$ (46.50 nm) > MPF-CeO$_2$ (40.76 nm) > MPF (20.98 nm).
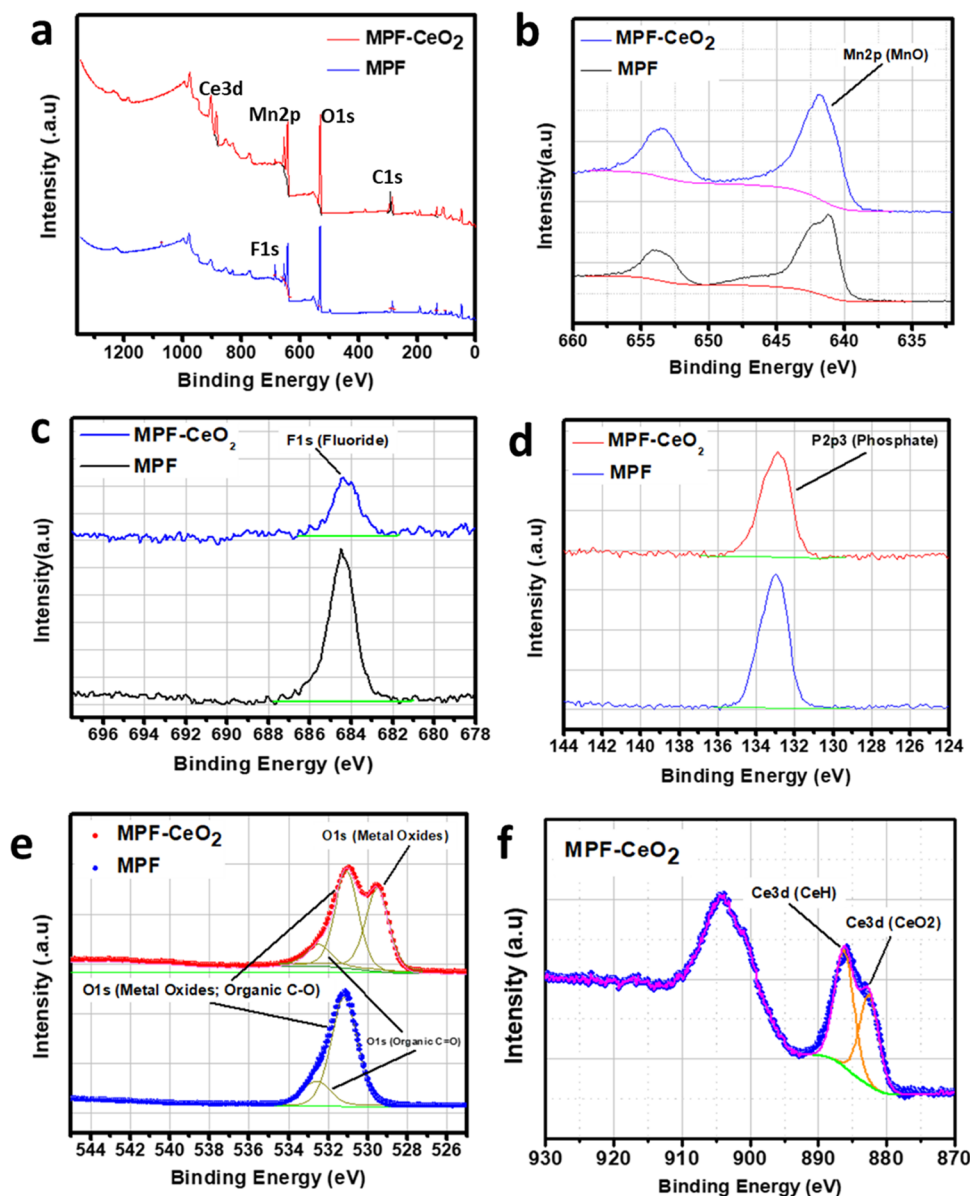
Figure 4. (a) Wide-range XPS spectra, (b) Mn 2p, (c) F 1s, (d) P $2p_{3/2}$, (e) O 1s, and (f) Ce 3d.

Similarly, as should be expected from the field-emission scanning electron microscopy (FESEM) images, the BET surface area of MPF-C-CeO_2 ($\sim$17 m^2 g^{-1}) is higher than those of the others ($\sim$13.6 and 1.6 m^2 g^{-1} for MPF-CeO_2 and MPF, respectively). A sharp rise in the N_2 gas adsorption volume is indicative of the formation of secondary mesopores arising from particle aggregation (as also observed in the SEM and TEM images) with MPF-CeO_2 reaching nearly 90 cm^3 g^{-1} and MPF-C-CeO_2 reaching $\sim$120 cm^3 g^{-1} of gas adsorption due to the ceria coating and carbon coating that further envelope the materials by forming a protective shell coating causing particle aggregation.

The XPS data are summarized in Figure 4 (showing typical XPS data for MFP and MFP-CeO_2, comparing the (a) survey scans, (b) Mn 2p, (c) F 1s, (d) P $2p_{3/2}$, (e) O 1s, and (f) Ce $3d_{5/2}$) and in Figure S8 (showing complimentary XPS data for MPF-C-CeO_2). As summarized in Table S4a–c, all of the elements are observed and exhibit peaks at their expected binding energy positions, with the CeO_2 coating showing no significant interference. The presence of the metal oxide (in

the 641.5–641.8 eV range) should be expected considering the Mn–O bond in the crystal structure of triplite. The fluoride F 1s peaks are observed in the 684.1–684.8 eV region, the phosphate P $2p_{3/2}$ appeared in the 133.0–133.9 eV range, while the O 1s appeared in the 528–534 eV range. The deconvoluted O 1s peak for MPF at 531.1 eV is attributed to the metal oxides and organic C=O, while the peak positioned at 532.6 is attributed to the organic C=O. The CeO_2-coated samples show a split O 1s peak (Figure 4e) attributed to metal oxide and metal oxide/organic oxide. The identification of Mn 2p and O 1s on the materials confirms the presence of the manganese atoms that lie at the centers of the highly distorted octahedra, coordinated by four O atoms.

Indeed, XPS clearly confirms that Mn and O are both bonded together to form metal oxides. Ce 3d (CeO_2) is positioned at 882.5 eV, and another Ce 3d (CeH) is positioned at 886.2 eV. In summary, the XPS data corroborate the XRD, Raman, and FTIR data, confirming the successful synthesis of mineral triplite (Mn_2PO_4F) using the microwave-assisted synthesis method and coating with a ceria thin film.
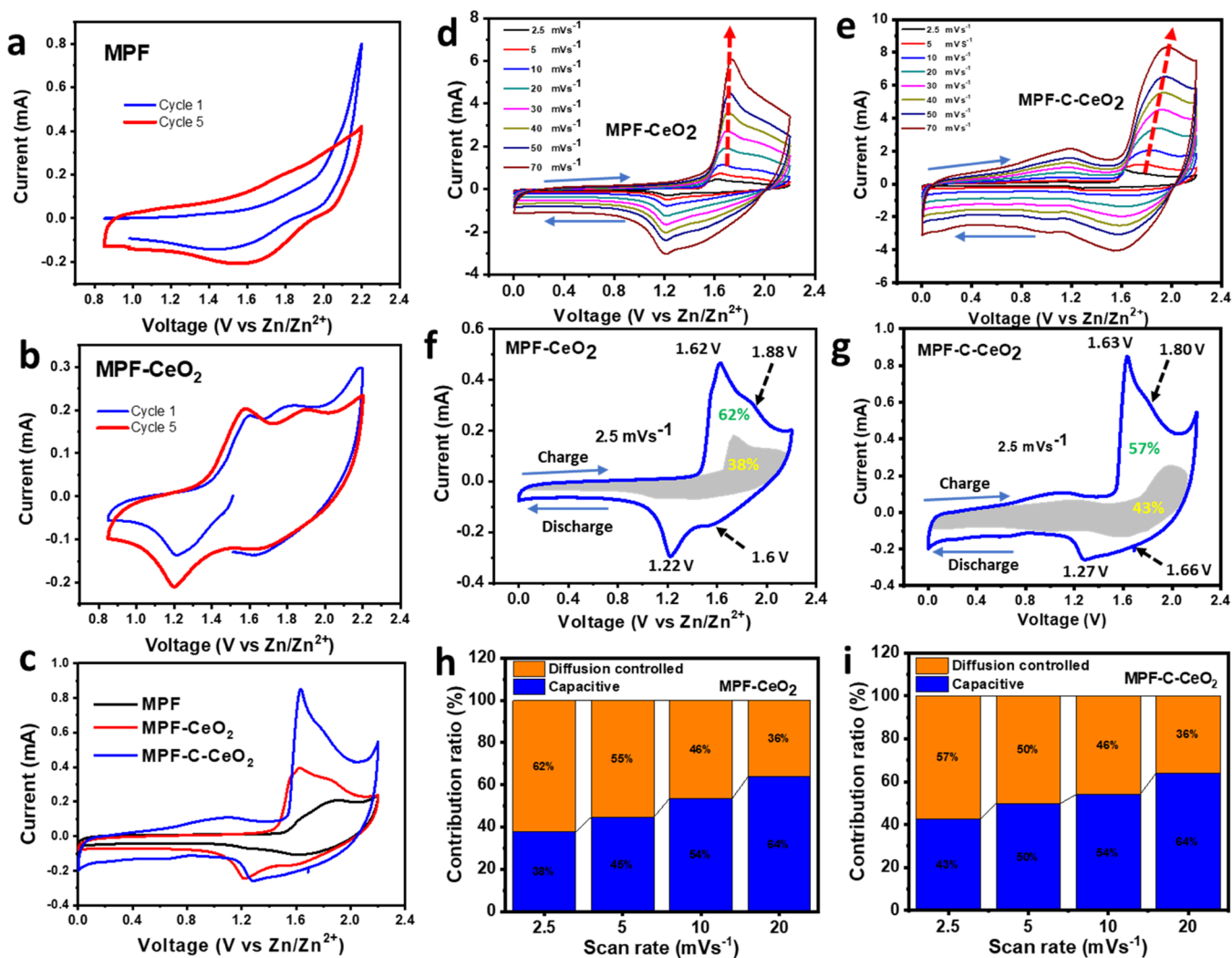
Figure 5. CV curves at different scan rates (2.5−70 mV s^{-1}) obtained after stable voltammograms have been obtained following repetitive galvanostatic charge−discharge and CV scanning for (a) MPF, (b) MPF-CeO$_2$, and (c) MPF-C-CeO$_2$; typical scan rate studies for (d) MPF-CeO$_2$ and (e) MPF-C-CeO$_2$ from 2.5 to 70 mV s^{-1}; typical CV curves with the capacitive contribution fractions depicted by the shaded area at a scan rate of 2.5 mV s^{-1} for (f) MPF-CeO$_2$ and (g) MPF-C-CeO$_2$; and contribution ratios at different scan rates (2.5−20 mV s^{-1}) for (h) MPF-CeO$_2$ and (i) MPF-C-CeO$_2$.

3.2. Electrochemical Analysis. Considering that there is no known literature on the redox or electrochemical properties of the MPF, this work first sought to understand the cyclic voltammetric (CV) properties of the three MPF-based materials for electrical energy storage. Figure 5 represents cyclic voltammograms of the three materials obtained using the Swagelok T-cell configuration with 4 M NaClO$_4$ as the electrolyte. Figure 5a,b presents typical cyclic voltammograms of MPF and MPF-CeO$_2$ obtained between 0.8 and 2.2 V after five repetitive CV scanning cycles. However, upon multiple cycles, especially with galvanostatic charge−discharge (GCD), the pristine MPF could be activated but hardly retains electrochemical stability. Unlike the ceria-based MPF, the pristine MPF did not show any detectable redox, meaning that it is difficult to activate the sodiation and desodiation process in the pristine MPF without ceria coating. Figure 5c compares the cyclic voltammograms of the three materials obtained between 0.0 and 2.2 V after five repetitive GCD at ∼12 mA g^{-1}, showing that the ceria and ceria−carbon coatings improve the redox behavior of the MPF. Note that the pristine MPF showed a small redox response after the GCD scan but this was

found to be unstable compared to the MPF-CeO$_2$ and MPF-C-CeO$_2$ compounds (also refer to Figures S9 and S10). The CV curves generally present interesting features. First, each of the materials can be operated in a large voltage window, up to 2.2 V, which is unusual for an aqueous electrolyte. This can partly be attributed to the inherent redox properties of Mn and partly to the use of the water-in-salt electrolyte, which is known to reduce the activity of water and expands the voltage window for enhanced safety and environmental sustainability.[28−31] Note that Mn-based electrodes for energy storage are known for their high energy, even in aqueous electrolytes.

Second, the CV curves provide insights into the structural stability of cells based on MPF-CeO$_2$ (Figure 5d) and MPF-C-CeO$_2$ (Figure 5g) during electrochemical cycling. From the CV curves, as the scan rate increases, the peak current increases, which is indicative of a diffusion-controlled redox process. At any given scan rate, the MPF-C-CeO$_2$ gives a higher current response than MPF-CeO$_2$. Also, as the scan rate increases, the anodic peaks of the MPF-C-CeO$_2$ increase and shift to the right, while those of MPF-CeO$_2$ remain unchanged (indicated by the dotted red arrows). For example, at 2.5 mV

s^{-1}, the anodic peak potential (E_{ap}) was ~1.7 V for all of the three electrode materials. However, at 70 mV s^{-1}, the E_{ap} value was 1.9 V for MPF-C-CeO$_2$ but remained 1.7 V for MPF-CeO$_2$. The shift in potential indicates that MPF-CeO$_2$ exhibits better charge-transfer kinetics than MPF-C-CeO$_2$. This behavior of the CV curves at different sweep rates provides some insights into the cycling stability and redox kinetics of the MPF-based electrode materials and indicates that MPF-CeO$_2$ exhibits the best structural and cycling stability as well as faster charge transport than others.
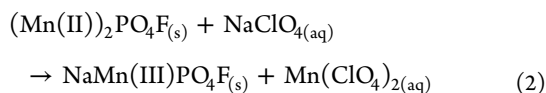
Third, at 2.5 mV s^{-1}, for example, each cell showed a well-defined redox couple at the equilibrium potential ($E^{1/2}$) at ca. 1.42 V for MPF-CeO$_2$ and 1.45 V vs Zn/Zn^{2+} for MPF-C-CeO$_2$, with weak redox couples appearing at around 1.7 V.

Based on the established knowledge of the redox chemistries of manganese compounds,[32−36] CeO$_2$[37] and MnO$_2$/CeO$_2$,[38,39] it is proposed that the well-defined redox couple from the CV curves at $E^{1/2} \approx 1.5$ V vs Zn/Zn^{2+} is related to the sodiation−desodiation process involving the Mn(II)/Mn(III) and/or Mn(III)/Mn(IV) redox processes (eqs 1−5), while the broad weak redox couple at ca. 1.7 V is related to the Ce(IV)/Ce(III) redox process (eq 6) as well as the surface adsorption−desorption process (eq 7). The contribution of the advantageous properties of Zn/Zn^{2+} (described in Section 1 and in eq 8) may not be ruled out.
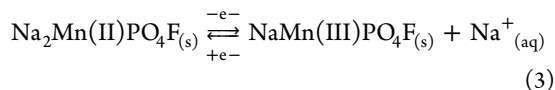
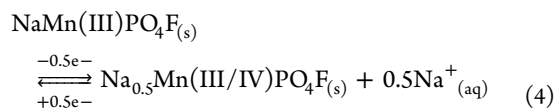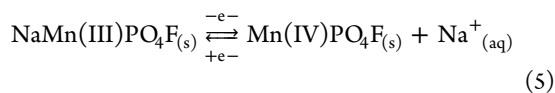(i) Initial process (electrosynthesis: ion-exchange, displacement reaction)

$$(Mn(II))_2PO_4F_{(s)} + 2NaClO_{4(aq)}$$
$$\rightarrow Na_2Mn(II)PO_4F_{(s)} + Mn(ClO_4)_{2(aq)} \quad (1)$$

or

$$(Mn(II))_2PO_4F_{(s)} + NaClO_{4(aq)}$$
$$\rightarrow NaMn(III)PO_4F_{(s)} + Mn(ClO_4)_{2(aq)} \quad (2)$$
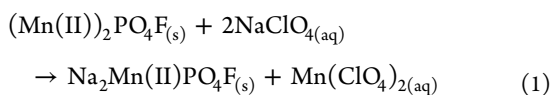
(ii) Desodiation−sodiation processes

$$Na_2Mn(II)PO_4F_{(s)} \underset{+e-}{\overset{-e-}{\rightleftharpoons}} NaMn(III)PO_4F_{(s)} + Na^+_{(aq)} \quad (3)$$

then

$$NaMn(III)PO_4F_{(s)}$$
$$\underset{+0.5e-}{\overset{-0.5e-}{\rightleftharpoons}} Na_{0.5}Mn(III/IV)PO_4F_{(s)} + 0.5Na^+_{(aq)} \quad (4)$$

or finally

$$NaMn(III)PO_4F_{(s)} \underset{+e-}{\overset{-e-}{\rightleftharpoons}} Mn(IV)PO_4F_{(s)} + Na^+_{(aq)} \quad (5)$$

(iii) Ceria faradic and nonfaradic processes

$$\text{faradaic: } Ce^{(IV)}O_{2(s)} + Na^+_{(aq)} \underset{-e-}{\overset{+e-}{\rightleftharpoons}} Ce^{(III)}O \cdot ONa_{(s)} \quad (6)$$

$$\text{nonfaradaic: } (Ce^{(IV)}O_2)_{(surface)} + Na^+_{(aq)}$$
$$\underset{-e-}{\overset{+e-}{\rightleftharpoons}} (Ce^{(IV)}O_2 \cdot Na)_{(surface)} \quad (7)$$
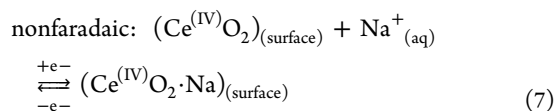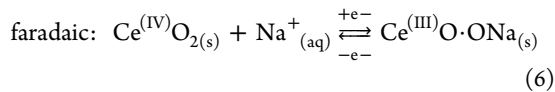
(iv) Anodic processes

$$Zn_{(s)} \underset{+2e-}{\overset{-2e-}{\rightleftharpoons}} Zn^{2+}_{(aq)} \quad (8)$$

Preliminary XRD investigations obtained after the galvanostatic charge−discharge cycling (Figure S11) suggest the formation of the Na complexes (i.e., Na$_2$Mn(II)PO$_4$F and NaMn(III)PO$_4$F) as proposed in eqs 1 and 2. This is an indication that the MPF open framework permits the insertion reaction with the sodium ion from the NaClO$_4$ electrolyte. This result agrees with the recent work by the Cui group,[40] which showed that the copper hexacyanoferrate (Cu$^{(II)}$−NC−Fe$^{(II/III)}$) open framework undergoes insertion reactions with sodium ions from the NaClO$_4$ electrolyte. Also, preliminary density functional theory (DFT) calculations show that it is thermodynamically more feasible to form Mn$_2$PO$_4$F (binding energy = −173.06067 eV) than to form the Na$_2$MnPO$_4$F (binding energy = −396.81173 eV) (Figure S12 and Table S5). The ability of sodium ions to be inserted/extracted from the open-framework structure of the MPF is also possible (Figure S13). The DFT result further confirms that eq 1 is possible and could perhaps be the rate-determining step in the redox steps.

Fourth, the CV curves of the MPF-based materials are characteristic of energy-storage electrode materials. The energy-storage mechanism of the MPF-based electrodes is the consequence of diffusion-controlled kinetics (i.e., faradic, batterylike process) or surface-confined kinetics (i.e., nonfaradic, capacitive process) or both. In other words, the current response is a contribution from capacitive (i_{cap}) and diffusive (i_{diff}) currents. Using the conventional power law equation (eqs 9 and 10), $i(V)$ is given as

$$i(V) = i_{cap} + i_{diff} = av^b \quad (9)$$

i.e., $\log i(V) = b \log v + \log a \quad (10)$

where v is the scan rate (V s^{-1}) and a and b are the adjustable parameters, with the value of b representing the slope of the linear curve, $\log i(V)$ vs $\log v$. If the value of b is 0.5, it indicates an ionic diffusion-controlled process, if it is 1.0, it means a pure capacitive process, but if the value is greater than 0.5 but less than 1.0, it suggests mixed kinetics (pseudocapacitive process). From a detailed analysis, the approximate b values range between 0.50 and 0.90, indicating that the electrochemical reactions of the CeO$_2$-coated MPF electrodes are controlled by ionic diffusion and pseudocapacitive processes. This finding agrees with the galvanostatic charge−discharge curves for the CeO$_2$-coated MPF cells that clearly exhibit battery-type behavior with high rate performance. In addition, the contribution from the capacitive process can be quantified from Dunn's method,[36,41] eqs 11 and 12

$$i(V) = k_1v + k_2v^{1/2} \quad (11)$$

which can be rearranged as

$$i(V)/v^{1/2} = k_1u^{1/2} + k_2 \quad (12)$$

where k_1v represents the capacitive contribution, while $k_2v^{1/2}$ is the ionic diffusion contribution. From the plots of $i(V)/v^{1/2}$ vs $v^{1/2}$, k_1 could be evaluated. As exemplified in Figure 5e,h, the capacitive contributions were obtained as 38% (MPF-CeO$_2$) and 43% (MPF-C-CeO$_2$) at 2.5 mV s^{-1}. However, as the scan rates increased, the capacitive contributions also increased (Figure 5f,i), increasing up to 64% at 20 mV s^{-1} for both MPF-
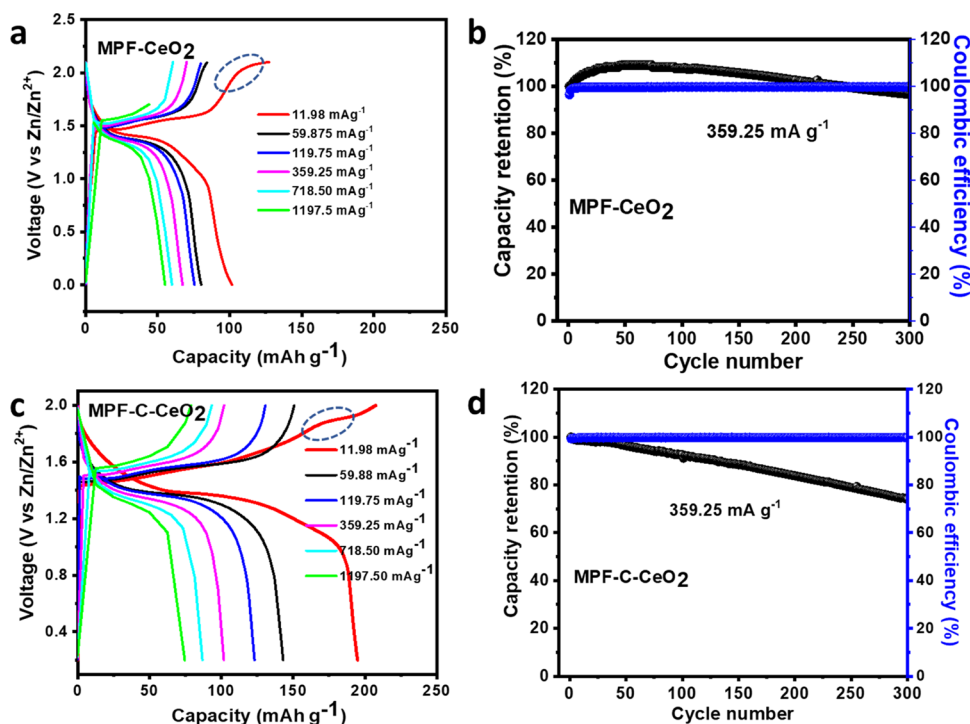
Figure 6. Rate performance of (a) MPF-CeO$_2$ and (c) MPF-C-CeO$_2$ obtained from 11.98 to 1197 mA g^{-1} and corresponding cycling stability and Coulombic efficiency of (b) MPF-CeO$_2$ and (d) MPF-C-CeO$_2$ at 359.25 mA g^{-1}.

CeO$_2$ and MPF-C-CeO$_2$, confirming that these CeO$_2$-coated MPF cells possess favorable sites for adsorption−desorption of sodium ions (corroborating eq 7), leading to high charge-transfer kinetics (i.e., high rate performance).

Next, galvanostatic charge−discharge (GCD) was used to determine the batterylike properties. As shown in Figure 6, the GCD was conducted in 0.0−2.0 V at different current densities: 12−1198 mA g^{-1} for both MPF-CeO$_2$ (Figure 6a) and MPF-C-CeO$_2$ (Figure 6c). Note that the weak ceria redox peaks were also observed (dotted oblong in Figure 6a,c) as in the CV curves (Figure 5f,g). Indeed, the GCD reveals some interesting findings. First, both MPF-CeO$_2$ and MPF-C-CeO$_2$ gave an open-circuit voltage of ca. 1.5 V, which is in the range or even higher than the working voltage of most aqueous batteries such as rechargeable aqueous Ni-MH, Na-ion, Al-ion, K-ion, and Zn-ion batteries with working voltages between 0.8 and 1.4 V[4] (Table S6). As a proof of concept, the cells were able to light an light-emitting diode (LED) for a long period (Figure S14). Second, the MPF gave an extremely poor GCD response, with a discharge capacity of ~2 mAh g^{-1} at 12 and 60 mA g^{-1} (Figure S10). However, upon coating the MPF with CeO$_2$ (i.e., MPF-CeO$_2$), a discharge capacity of 104 mAh g^{-1} (energy of 156 Wh g^{-1}) was achieved at a current density of ~12 mA g^{-1}, which clearly indicates that CeO$_2$ acts as the key that unlocks the latent energy-storage capability of the MPF. MPF-CeO$_2$ gave a specific discharge capacity of ~105 mAh g^{-1}, while the incorporation of both carbon and ceria (MPF-C-CeO$_2$-C) increased the specific discharge capacity to ~195 mAh g^{-1} at a current of ~12 mA g^{-1}.

The difference in the electrochemical performance between MPF-CeO$_2$ and MPF-C-CeO$_2$ is attributed to the synergistic interaction between the conductive species, carbon and CeO$_2$, which introduces extra conductivity to the MPF (i.e., reduced impedance, confirmed by the EIS data as discussed later). Carbon and ceria can co-operatively increase the specific

discharge capacity of the MPF, which is consistent with the findings of Wang et al.,[42] who showed that the incorporation of CeO$_2$ nanoparticles onto the surface of carbon nanotubes leads to enhanced space charge polarization, interfacial polarization, and conductivity (reduced impedance) due to the supply of oxygen vacancies by the CeO$_2$ nanoparticles.

Third, the two ceria-based MPF materials (i.e., MPF-CeO$_2$ and MPF-C-CeO$_2$) gave excellent rate capability. For example, even at a very high current density (1198 mA g^{-1}) MPF-CeO$_2$ still gave 58 mAh g^{-1} (i.e., 55.8% of its initial discharge capacity of 104 mAh g^{-1}), while MPF-C-CeO$_2$ gave 60 mAh g^{-1} (i.e., 37.7% of its initial discharge capacity of 199 mAh g^{-1}). This result indicates that MPF-CeO$_2$ exhibits better cycling stability than its MPF-C-CeO$_2$ counterpart. The cycling stability of the cells is further interrogated using repetitive GCD (Figure 6b,d), which consistently confirmed that the MPF-CeO$_2$ cell shows higher stability than MPF-C-CeO$_2$. The repetitive GCD, conducted up to 300 cycles, shows that MPF-CeO$_2$ is more stable than MPF-C-CeO$_2$, which perfectly corroborates the scan rate studies (shown in Figure 5b,g). In general, the high structural stability of MPF-CeO$_2$ compared to that of the pristine MPF is due to the strong interaction between Mn and Ce because of the higher electrophilic index of Mn (1.55) than that of Ce (1.12), which makes it possible for electrons to be transferred from the Ce to Mn.[38,39]

The decreased cycling stability of MPF-C-CeO$_2$ compared to that of MPF-CeO$_2$ could be attributed to the differences in the morphologies of these two samples; micron-sized aggregated nanoparticles (MPF-CeO$_2$) vs high-surface-area nanoporous material (MPF-C-CeO$_2$). It is well known that micron-sized cathode materials provide better electrochemistry for battery and batterylike systems than the nanosized cathode materials.[43−45] Nanoparticulate electrode materials are fraught with twofold disadvantages. First, due to their inherent high specific surface area, nanosized electrode materials are
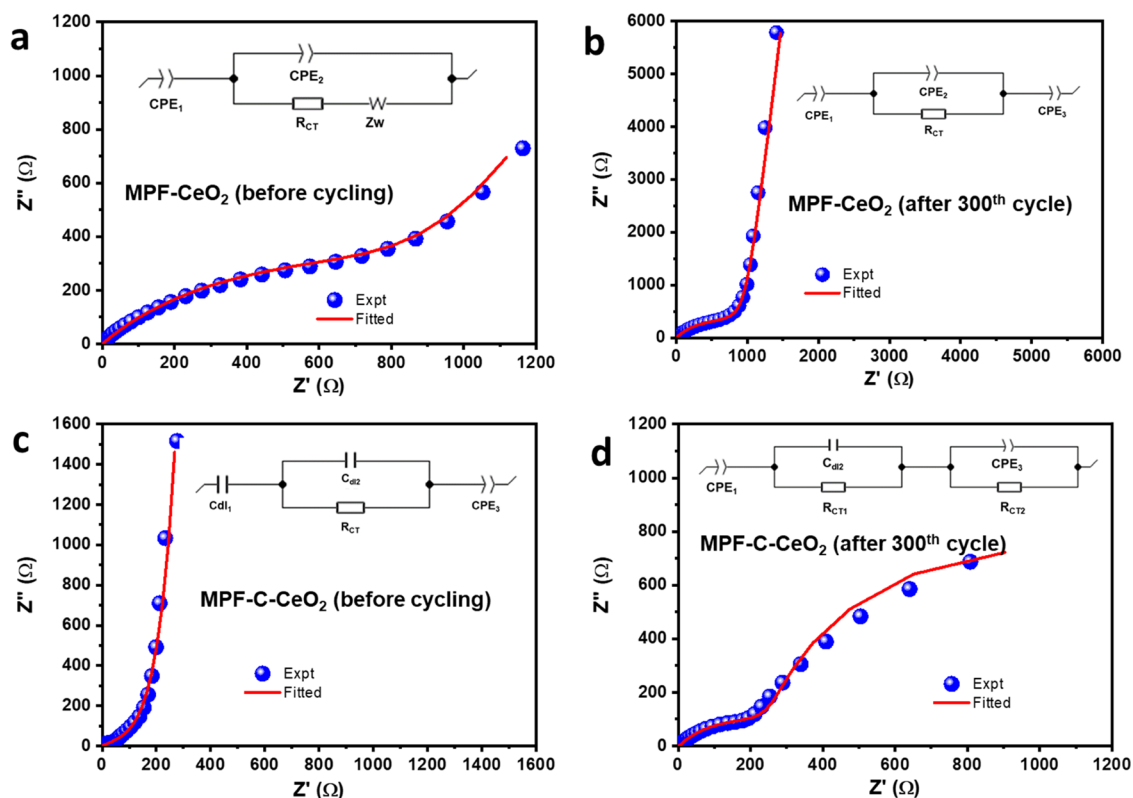
Figure 7. Nyquist plots of MPF-CeO$_2$ (a) before cycling and (b) after the 300th cycle and MPC-C-CeO$_2$ (c) before cycling and (d) after the 300th cycle. Insets are the electrical equivalent circuits used to fit the respective experimental Nyquist plots.

characterized by their high reactivity (i.e., promotes side reactions with electrode additives and electrolytes), leading to irreversible capacity loss and poor cycling performance. Second, nanosized electrode materials exhibit poor tapping density, which makes it difficult for them to be densely packed on the current collector as micron-sized electrode materials. For example, Li et al.[44] showed that nanostructured LiCoO$_2$ cathode material for lithium-ion batteries was able to deliver high initial capacity; however, its capacity retention was only 74% after 80 cycles. Thus, the poor cycling performance of MPF-C-CeO$_2$ is due to its high specific surface area and nanoporous structure that confer high electrode reactivity, leading to faster electrode decomposition compared to MPF-CeO$_2$. Therefore, there is a need to optimize the carbon/ceria content in MPF-C-CeO$_2$ with the view to harnessing its high capacity but without compromising on its cycling stability.

When compared to many other aqueous batteries (see Table S6), the MPF-based battery reported in this work provide better results, especially in terms of working voltage, specific capacity, and capacity retention. For example, the recent work by Suo et al.,[29] on a rechargeable aqueous Na-ion battery based on Na$_{0.66}$[Mn$_{0.66}$Ti$_{0.34}$]O$_2$ as the cathode and NaTi$_2$(PO$_4$)$_3$ with water-in-salt electrolyte showed ~1.1 V and ~30 mAh g^{-1}. Indeed, the MPF-based materials provide excellent promise for the development of low-cost and high-performance next-generation aqueous battery technologies. Importantly, the carbon–ceria system that provides higher capacity would require more studies with the view to improving its long cycling stability.

It is well established that ceria coating confers good electrochemical properties to the cathode materials for energy-storage systems (including sodium- and lithium-ion

batteries) in terms of structural stability, cycling stability, rate capability, and capacity retention. In our case, we believe that the ability of ceria to activate the MPF to store electric energy may be related to its inherent physicochemical properties of CeO$_2$: the strong interaction of Ce and Mn, good protection against corrosion, good ionic conductivity, reversible oxygen storage, and catalytic activity. In addition, CeO$_2$ is a three-dimensional (3-D) open-framework, fluorite-structured ceramic that exhibits a highly stable crystallographic morphology at a high temperature.[46] It provides the advantage of protecting cathode materials from corrosive aprotic electrolytes. Thus, it may be assumed that the open-framework structure of the MPF is protected and stabilized by the open 3-D fluorite-structured ceria, thereby allowing a reversible extraction/insertion of the Na ion.

EIS is a powerful technique that permits one to decouple the electrochemical events that occur at different timescales.[47−50] Thus, EIS experiments were conducted before and after 300 repetitive cycles to provide further insights into the electrochemical properties of the MPF-CeO$_2$ and MPF-C-CeO$_2$ battery cells. From the Nyquist plots of the MPF-CeO$_2$ cells, three different events are observed before (Figure 7a) and after (Figure 7b) the 300th cycle at the high-frequency (HF, ~100 kHz), mid-frequency (MF, ~600 Hz), and low-frequency (LF, ~0.01 Hz) regions. Before cycling of MPF-CeO$_2$, the simulated components include a constant-phase element (CPE$_1$) at HF due to the capacitance of the electrode/electrolyte interface; a semicircular arc at the MF is due to the charging of the electrode/electrolyte interface. It consists of the Randles electrical equivalent circuit (EEC), comprising CPE$_2$, charge-transfer resistance (R_{CT}), and a linear region inclined at about 45° due to the Z_w (i.e., Warburg impedance

Table 1. EIS Parameters for MPF-CeO$_2$ and MPF-C-CeO$_2$ before and after 300 Electrochemical Cycling Experiments

EIS parameter	MPF-CeO$_2$		MPF-C-CeO$_2$	
	before cycling	after the 300th cycle	before cycling	after the 300th cycle
CPE$_1$ (F s^{n-1})	7.27 ± 1.12	3.18 ± 0.01		2.99 ± 0.16
a_1	0.35	0.43		0.40
CPE$_2$ (mF s^{n-1})	0.448 ± 0.01	0.24 ± 0.01		
a_2	0.74	0.68		
R_{CT} (R_{CT1}) (Ω)	413 ± 19.48	660 ± 9.10	9.53 ± 1.35	718.1 ± 73.88
Z_w (Ω s$^{-0.5}$)	133.2 ± 7.10			
C_{dl1} (mF)			12.3 ± 0.03	
C_{dl2} (mF)			0.26 ± 0.07	10.3 ± 0.40
R_{CT2} (Ω)				68.95 ± 13.2
CPE$_3$ (mF s^{n-1})		3.16 ± 0.03	7.62 ± 0.07	0.36 ± 0.15
a_3		0.99	0.33	0.88

due to the Na-ion diffusion process). After the 300th cycle of MPF-CeO$_2$ (Figure 7b), the Nyquist plot shows CPE$_1$ connected to the RC circuit (i.e., CPE$_2$ and R_{CT}).

Note that the R_{CT} represents contributions from both electronic- and ionic-transfer resistances; the frequency resolution is highly limited that the exact contribution from electronic and ionic cannot be decoupled; thus, the sum is represented by a single parameter. At the LF region, a near-vertical spike, like that of a pure capacitor alone, is observed (represented as CPE$_3$). Such a spike usually occurs at frequencies lower than about 10 Hz and is attributed to the build-up of charge at the electrode−electrolyte interface, charge accumulation. Thus, the CPE at 0.01 Hz is due to the accumulation of Na-ion charges at the electrode−electrolyte interface. The increased R_{CT} value of MPF-CeO$_2$ (from 413 to 660 Ω after the 300th cycle) depicts the deterioration of the electrode/electrolyte interface as the number of cycles increased. These changes in frequencies are clearly visible in the Bode plot (Figure S15).

For the MPF-C-CeO$_2$ cell (Figure 7c,d), prior to cycling (Figure 7c), the EEC is essentially the same as that of MPF-CeO$_2$ before cycling (Figure 7a), except that MPF-C-CeO$_2$ exbibits more of a pure capacitive process (double-layer capacitance (C_{dl}) compared to the more pseudocapacitive behavior (CPE) of MPF-CeO$_2$). In addition, as should be expected of the effect of combining the conductive carbon and ceria species, MPF-C-CeO$_2$ gave higher conductivity (low R_{CT} value, ∼9.5 Ω) than MPF-CeO$_2$ (total R_{CT} in series, 660 Ω). At the end of the 300th cycle, MPF-C-CeO$_2$ is fitted with a Voigt-type EEC, comprising CPE$_1$ at HF as described for others, R_{CT1}/CPE$_2$ at MF, and R_{CT2}/CPE$_3$ at LF. The increased R_{CT} value of MPF-C-CeO$_2$ (from 9.5 to 787 Ω after the 300th cycle) depicts a more intense deterioration of the electrode/electrolyte interface as the number of cycles increased compared to the MPF-CeO$_2$ cell. These changes in frequencies are clearly visible in the Bode plot (Figure S14).

CPE arises from the inhomogeneous nature of the electrode surface, i.e., a rough or irregular and porous surface structure. CPE is frequently used as a substitute for a pure capacitor or double-layer capacitor. The impedance of the CPE (Z_{CPE}) is defined in eq 13[47−50]

$$Z_{CPE} = 1/Q(j\omega)^n \tag{13}$$

where Q is the nonideal capacitance (in the unit of F s^{n-1}) and n defines the ideality factor with values in the −1 and +1 range (i.e., $-1 \leq n \leq 1$): when $n = 0$, the Z_{CPE} represents a pure resistor; when $n = 1$, the Z_{CPE} is the same as a pure capacitor; when $n = -1$, the Z_{CPE} is a pure inductor; when $n = 0.5$, the Z_{CPE} represents the Warburg impedance. For example, in Table 1, the value of $n = 0.88$ indicates the pseudocapacitive properties of MPF-C-CeO$_2$ after the 300th cycle, in contrast to the $n = 0.33$ for MPF-C-CeO$_2$ before cycling, indicating a somewhat resistive interface.

4. CONCLUSIONS

In summary, this work describes how a virtually unknown triplite material can be manipulated to unlock its energy-storage potential by adopting a ceria coating and a simple microwave-assisted synthesis method. The CeO$_2$ coating improves the electrochemical performance of cathode materials by several factors, including the stabilization of the electrode structure, protecting the electrode from the etching effect of the electrolyte, improving the ionic conductivity of the electrode, reversible oxygen storage, and induced catalytic activity that enhances the redox behavior of the electrode. In this work, as also seen in the literature, moderate CeO$_2$ coating (∼2 wt %) with uniform distribution (evident from EDX mapping), coating thickness (between 0.291 and 3.56 μm), aided by inclusion of conductive carbon for reduced interfacial impedance, provides the best electrochemical performance of the MPF. MPF-CeO$_2$ gave better cycling stability compared to MPF-C-CeO$_2$ due to the differences in the morphologies; thus, there is a need to optimize the carbon/ceria content in MPF-C-CeO$_2$ with the view to harnessing its high capacity but without compromising on its cycling stability. The findings in this study open a new window of research and innovation opportunities for triplite-based energy-storage materials for large-scale development of a plethora of low-cost, high-energy, and high-power rechargeable aqueous mobile-ion batteries. The new triplite cathode material adds value to the search for a next-generation low-cost, lithium-free, high-performance battery technology. Indeed, this work provides significant insight into ceria-based triplite for the development of new energy-storage systems.

■ ASSOCIATED CONTENT

ⓢ Supporting Information

The Supporting Information is available free of charge at https://pubs.acs.org/doi/10.1021/acsaem.1c02734.

> Synthesis schemes, FESEM images, HRTEM images, EDX elemental mapping images, calculation of d-spacings, FTIR spectra, nitrogen adsorption−desorption isotherms, XPS data, description of cyclic voltammetric

evolutions pre- and postgalvanostatic charge—discharge experiments, XRD data after galvanostatic charge—discharge (GCD) experiments, DFT simulation methodologies, proof of concept showing the ability of MPF-C-CeO$_2$ to light an LED (1.62 V), and Bode plots for the EIS data (PDF)

■ AUTHOR INFORMATION

Corresponding Author

Kenneth I. Ozoemena − *Molecular Sciences Institute, School of Chemistry, University of the Witwatersrand, Johannesburg 2050, South Africa;* ⊙ orcid.org/0000-0001-7107-7003; Phone: +27 11 7176730; Email: kenneth.ozoemena@wits.ac.za

Authors

Nkosikhona Nzimande − *Molecular Sciences Institute, School of Chemistry, University of the Witwatersrand, Johannesburg 2050, South Africa*

Aderemi Haruna − *Molecular Sciences Institute, School of Chemistry, University of the Witwatersrand, Johannesburg 2050, South Africa*

Patrick Mwonga − *Molecular Sciences Institute, School of Chemistry, University of the Witwatersrand, Johannesburg 2050, South Africa*

Bertold Rasche − *Department of Chemistry, University of Cologne, 50939 Köln, Germany*

Franscious Cummings − *Electron Microscope Unit, Department of Physics and Astronomy, University of the Western Cape, Bellville 7535, South Africa*

Complete contact information is available at:
https://pubs.acs.org/10.1021/acsaem.1c02734

Author Contributions

K.I.O., conception, interpretation of data, writing, and supervision of students. N.N., conception, experimentation, interpretation of data, and writing. A.H., experimentation, interpretation of data, writing. P.M., DFT modeling. B.R., XRD data, interpretation of data, and writing. F.C., HRTEM data. All authors have given approval to the final version of the manuscript.

Notes

The authors declare no competing financial interest.

■ ACKNOWLEDGMENTS

■ REFERENCES

(1) Armand, M.; Tarascon, J. M. Building better batteries. *Nature* **2008**, *451*, 652−657.

(2) Dunn, B.; Kamath, H.; Tarascon, J. M. Electrical energy storage for the grid: a battery of choices. *Science* **2011**, *334*, 928−935.

(3) Manthiram, A. A reflection on lithium-ion battery cathode chemistry. *Nat. Commun.* **2020**, *11*, No. 1550.

(4) Chao, D.; Zhou, W.; Xie, F.; Ye, C.; Li, H.; Jaroniec, M.; Qiao, S.-Z. Roadmap for advanced aqueous batteries: From design of materials to applications. *Sci. Adv.* **2020**, *6*, No. eaba4098.

(5) Nian, Q.; Liu, S.; Liu, J.; Zhang, Q.; Shi, J.; Liu, C.; Wang, R.; Tao, Z.; Chen, J. All-Climate Aqueous Dual-Ion Hybrid Battery with Ultrahigh Rate and Ultralong Life Performance. *ACS Appl. Energy Mater.* **2019**, *2*, 4370−4378.

(6) Abraham, K. M. How Comparable Are Sodium-Ion Batteries to Lithium-Ion Counterparts. *ACS Energy Lett.* **2020**, *5*, 3544−3547.

(7) Hwang, J.-Y.; Myung, S.-T.; Sun, Y.-K. Sodium-ion batteries: present and future. *Chem. Soc. Rev.* **2017**, *46*, 3529−3614.

(8) Zhao, Z.; Fan, X.; Ding, J.; Hu, W.; Zhong, C.; Luc, J. Challenges in zinc electrodes for alkaline zinc−air batteries: Obstacles to commercialization. *ACS Energy Lett.* **2019**, *4*, 2259−2270.

(9) Lai, J.; Zhu, H.; Zhu, X.; Koritala, H.; Wang, Y. Interlayer-Expanded V6O13·nH2O Architecture Constructed for an Advanced Rechargeable Aqueous Zinc-Ion Battery. *ACS Appl. Energy Mater.* **2019**, *2*, 1988−1996.

(10) Wan, F.; Zhang, L.; Dai, X.; Wang, X.; Niu, Z.; Chen, J. Aqueous rechargeable zinc/sodium vanadate batteries with enhanced performance from simultaneous insertion of dual carriers. *Nat. Commun.* **2018**, *9*, No. 1656.

(11) Wang, F.; Borodin, O.; Gao, T.; Fan, X.; Sun, W.; Han, F.; Faraone, A.; Dura, J. A.; Xu, K.; Wang, C. Highly reversible zinc metal anode for aqueous batteries. *Nat. Mater.* **2018**, *17*, 543−549.

(12) Ko, J. S.; Bishop, K.; Seitzman, N.; Chen, B.-R.; Toney, M. F.; Weker, J. N. Highly Reversible Plating/Stripping of Porous Zinc Anodes for Multivalent Zinc Batteries. *J. Electrochem. Soc.* **2020**, *167*, No. 140520.

(13) Rea, J. R.; Kostiner, E. The Crystal Structure of Manganese Fluorophosphate, Mn$_2$(PO$_4$)F. *Acta Crystallogr., Sect. B: Struct. Crystallogr. Cryst. Chem.* **1972**, *28*, 2525.

(14) Makgopa, K.; Ejikeme, P. M.; Jafta, C. J.; Raju, K.; Zeiger, M.; Presser, V.; Ozoemena, K. I. A high-rate aqueous symmetric pseudocapacitor based on highly graphitized onion-like carbon/birnessite-type manganese oxide nanohybrids. *J. Mater. Chem. A* **2015**, *3*, 3480−3490.

(15) Raju, K.; Han, H.; Velusamy, D. B.; Jiang, Q.; Yang, H.; Nkosi, F. P.; Palaniyandy, N.; Makgopa, K.; Bo, Z.; Ozoemena, K. I. Rational Design of 2D Manganese Phosphate Hydrate Nanosheets as Pseudocapacitive Electrodes. *ACS Energy Lett.* **2020**, *5*, 23−30.

(16) Makgopa, K.; Raju, K.; Ejikeme, P. M.; Ozoemena, K. I. High-performance Mn3O4/onion-like carbon (OLC) nanohybrid pseudo-capacitor: Unravelling the intrinsic properties of OLC against other carbon supports. *Carbon* **2017**, *117*, 20−32.

(17) Jafta, C. J.; Mathe, M. K.; Manyala, N.; Roos, W. D.; Ozoemena, K. I. Microwave-Assisted Synthesis of High-Voltage Nanostructured LiMn1.5Ni0.5O4 spinel: Tuning the Mn3+ Content and Electrochemical Performance. *ACS Appl. Mater. Interfaces* **2013**, *5*, 7592−7598.

(18) Jafta, C. J.; Raju, K.; Mathe, M. K.; Manyala, N. I.; Ozoemena, K. I. Microwave Irradiation Controls the Manganese Oxidation States of Nanostructured (Li[Li$_{0.2}$Mn$_{0.52}$Ni$_{0.13}$Co$_{0.13}$Al$_{0.02}$]O$_2$) Layered Cathode Materials for High-Performance Lithium Ion Batteries. *J. Electrochem. Soc.* **2015**, *162*, A768−A773.

(19) Chae, M. S.; Kim, H. J.; Lyoo, J.; Attias, R.; Elias, Y.; Gofer, Y.; Hong, S.-T.; Aurbach, D. Boosting Tunnel-Type Manganese Oxide Cathodes by Lithium Nitrate for Practical Aqueous Na-Ion Batteries. *ACS Appl. Energy Mater.* **2020**, *3*, 10744−10751.

(20) Kelly, T. D.; Matos, G. R. *Historical Statistics for Mineral and Material Commodities in the United States*; US Geological Surveys: Washington, DC, 2010.

(21) Yao, J.; Wu, F.; Qi, X.; Li, N.; Su, Y. Effect of CeO$_2$-coating on the electrochemical performances of LiFePO4/C cathode material. *Electrochim. Acta* **2011**, *56*, 5587−5592.

(22) Liu, K.; Yang, G.-L.; Dong, Y.; Shi, T.; Chen, L. Enhanced cycling stability and rate performance of Li[Ni0.5Co0.2Mn0.3] O2 by CeO2 coating at high cut-off voltage. *J. Power Sources* **2015**, *281*, 370−377.

(23) Wang, Y.; Tang, T. CeO2-modified P2−Na−Co−Mn−O cathode with enhanced sodium storage characteristics. *RSC Adv.* **2018**, *8*, 24143−24153.

(24) Mangam, V.; Bhattacharya, S.; Das, K.; Das, S. Friction and wear behavior of Cu−CeO2 nanocomposite coatings synthesized by pulsed electrodeposition. *Surf. Coat. Technol.* **2010**, *205*, 801−805.

(25) Trovarelli, A. Catalytic properties of ceria and CeO2-containing materials. *Catal. Rev.* **1996**, *38*, 439−520.

(26) Waldrop, L. Crystal structure of triplite. *Naturwissenschaften* **1968**, *55*, 178.

(27) Vignola, P.; Gatta, G. D.; Hatert, F.; Guastoni, A.; Bersani, D. On the crystalchemistry of a near-endmember triplite, Mn2+2(PO4)-F, from the Codera Valley (Sondrio Province, Central Alps, Italy). *Can. Mineral.* **2014**, *52*, 235−245.

(28) Suo, L.; Borodin, O.; Gao, T.; Olguin, M.; Ho, J.; Fan, X.; Luo, C.; Wang, C.; Xu, K. Water-in-salt" electrolyte enables high-voltage aqueous lithium-ion chemistries. *Science* **2015**, *350*, 938−943.

(29) Suo, L.; Borodin, O.; Wang, Y.; Rong, X.; Sun, W.; Fanm, X.; Xu, S.; Schroeda, M. A.; Cresce, A. V.; Wang, F.; Yang, C.; Hu, Y.-S.; Xu, K.; Wang, C. Water-in-Salt electrolyte makes aqueous sodium-ion battery safe, green, and long-lasting. *Adv. Energy Mater.* **2017**, *7*, No. 1701189.

(30) Lukatskaya, M. R.; Feldblyum, J. I.; Mackanic, D. G.; Lissel, F.; Michels, D. L.; Cui, Y.; Bao, Z. Concentrated mixed cation acetate "water-in-salt" solutions as green and low-cost high voltage electrolytes for aqueous batteries. *Energy Environ. Sci.* **2018**, *11*, 2876−2883.

(31) Lin, C.-H.; Sun, K.; Ge, M.; Housel, L. M.; McCarthy, A. H.; Vila, M. N.; Zhao, C.; Xiao, X.; Lee, W.-K.; Takeuchi, K. J.; Takeuchi, E. S.; Marschilok, A. C.; Chen-Wiegart, Y.-C. K. Systems-level investigation of aqueous batteries for understanding the benefit of water-in-salt electrolyte by synchrotron nanoimaging. *Sci. Adv.* **2020**, *6*, No. eaay7129.

(32) Pan, H.; Shao, Y.; Yan, P.; Cheng, Y.; Han, K. S.; Nie, Z.; Wang, C.; Yang, J.; Li, X.; Bhattacharya, P.; Mueller, K. T.; Liu, J. Reversible aqueous zinc/manganese oxide energy storage from conversion reactions. *Nat. Energy* **2016**, *1*, No. 16039.

(33) Jiang, B.; Xu, C.; Wu, C.; Dong, L.; Li, J.; Kang, F. Manganese Sesquioxide as Cathode Material for Multivalent Zinc Ion Battery with High Capacity and Long Cycle Life. *Electrochim. Acta* **2017**, *229*, 422−428.

(34) Zhu, C.; Guozhao Fang, G.; Zhou, J.; Guo, J.; Wang, Z.; Wang, C.; Li, J.; Tang, Y.; Liang, S. Binder-free stainless steel@Mn3O4 nanoflower composite: a high-activity aqueous zinc-ion battery cathode with high-capacity and long cycle-life. *J. Mater. Chem. A* **2018**, *6*, 9677−9683.

(35) Chen, H.; Hao, Q.; Zivkovic, O.; Hautier, G.; Du, L.-S.; Tang, Y.; Hu, Y.-Y.; Ma, X.; Grey, C. P.; Ceder, G. Sidorenkite (Na3MnPO4CO3): A New Intercalation Cathode Material for Na-Ion Batteries. *Chem. Mater.* **2013**, *25*, 2777−2786.

(36) Yan, B.; Bin, D.; Ren, F.; Xiong, Z.; Zhang, K.; Wang, C.; Du, Y. Facile Synthesis of MnPO$_4$.H$_2$O Nanowire/Graphene Oxide Composite Material and Its Application as Electrode Material for High Performance Supercapacitors. *Catalysts* **2016**, *6*, No. 198.

(37) Maiti, S.; Pramanik, A.; Mahanty, S. Extraordinarily high pseudocapacitance of metal organic framework derived nanostructured cerium oxide. *Chem. Commun.* **2014**, *50*, 11717−11720.

(38) Zhang, H.; Gu, J.; Tong, J.; Hu, Y.; Guan, B.; Hu, B.; Zhao, J.; Wang, C. Hierarchical porous MnO2/CeO2 with high performance for supercapacitor electrodes. *Chem. Eng. J.* **2016**, *286*, 139−149.

(39) Zhou, J.; Wu, T.; Han, Y.; Aryana, S. Fabrication of Mn-Ce Bimetallic Oxides as Electrode Material for Supercapacitors with High Performance. *J. Electron. Mater.* **2021**, *50*, 2725−2737.

(40) Pasta, M.; Wessells, C. D.; Liu, N.; Nelson, J.; Mcdowell, M. T.; Huggins, R. A.; Toney, M. F.; Cui, Y. Full open-framework batteries for stationary energy storage. *Nat. Commun.* **2014**, *5*, No. 3007.

(41) Wang, J.; Polleux, J.; Lim, J.; Dunn, B. Pseudocapacitive contributions to electrochemical energy storage in TiO2 (anatase) nanoparticles. *J. Phys. Chem. C* **2007**, *111*, 14925−14931.

(42) Wang, H.; Xing, H.; Liu, Q.; Jia, H.; Chen, A.; Liu, Y. Synthesis and microwave absorbing properties of CeO2/multi-walled carbon nanotubes composites. *J. Mater. Sci.: Mater. Electron.* **2018**, *29*, 19308−19315.

(43) Okubo, M.; Hosono, E.; Kudo, T.; Zhou, H. S.; Honma, I. Size effect on electrochemical property of nanocrystalline LiCoO$_2$ synthesized from rapid thermal annealing method. *Solid State Ionics* **2009**, *180*, 612−615.

(44) Li, K.; Lin, S.; Shua, F.; Zhang, J.; Chen, K.; Xue, D. A rapid combustion route to synthesize high-performance nanocrystalline cathode materials for Li-ion batteries. *CrystEngComm* **2014**, *16*, 10969.

(45) Geder, J.; Hoster, H. E.; Jossen, A.; Garche, J.; Yu, D. Y. W. Impact of active material surface area on thermal stability of LiCoO2 cathode. *J. Power Sources* **2014**, *257*, 286−292.

(46) Kim-Lohsoontorn, P.; Tiyapongpattana, V.; Asarasri, N.; Seeharaj, P.; Laosiripojana, N. Preparation of CeO2 Nano Rods Through a Sonication-Assisted Precipitation. *Int. J. Appl. Ceram. Technol.* **2014**, *11*, 645−653.

(47) Bredar, A. R. C.; Chown, A. L.; Burton, A. R.; Farnum, B. H. Electrochemical Impedance Spectroscopy of Metal Oxide Electrodes for Energy Applications. *ACS Appl. Energy Mater.* **2020**, *3*, 66−98.

(48) Pillay, J.; Ozoemena, K. I. Layer-by-layer self-assembled nanostructured phthalocyaninatoiron(II)/SWCNT-poly(m-amino-benzenesulfonic acid) hybrid system on gold surface: Electron transfer dynamics and amplification of H$_2$O$_2$ response. *Electrochim. Acta* **2009**, *54*, 5053−5059.

(49) Ozoemena, K. I.; Mathebula, N. S.; Pillay, J.; Toschi, G.; Verschoor, J. A. Electron transfer dynamics across self-assembled N-(2-mercaptoethyl) octadecanamide/mycolic acid layers: impedimetric insights into the structural integrity and interaction with anti-mycolic acid antibodies. *Phys. Chem. Chem. Phys.* **2010**, *12*, 345−357.

(50) Chidembo, A. T.; Ozoemena, K. I.; Agboola, B. O.; Gupta, V.; Wildgoose, G. G.; Compton, R. G. Nickel(II)tetra-aminophthalocyanine modified MWCNTs as potential nanocomposite materials for the development of supercapacitors. *Energy Environ. Sci.* **2010**, *3*, 228−236.